Journal of The Electrochemical Society, **165** (9) F613-F620 (2018)
0013-4651/2018/165(9)/F613/8/$37.00 © The Electrochemical Society

Two-Phase Flow Dynamics in the Gas Diffusion Layer of Proton Exchange Membrane Fuel Cells: Volume of Fluid Modeling and Comparison with Experiment

Zhiqiang Niu,[1,2] Yun Wang,[2,*,z] Kui Jiao,[1,z] and Jingtian Wu[2]

[1] *State Key Laboratory of Engines, Tianjin University, Tianjin 300350, People's Republic of China*
[2] *Renewable Energy Resources Lab (RERL), Department of Mechanical and Aerospace Engineering, University of California, Irvine, California 92697-3975, USA*

This paper proposes a three-dimensional (3D) volume of fluid (VOF) study to investigate two-phase flow in the gas diffusion layer (GDL) of proton exchange membrane (PEM) fuel cells and liquid water distribution. A stochastic model was adopted to reconstruct the 3D microstructures of Toray carbon papers and incorporate the experimentally-determined varying porosity. The VOF predictions were compared with the water profiles obtained by the X-ray tomographic microscopy (XTM) and the Leverett correlation. It was found local water profiles are similar in the sample's sub-regions under the pressure difference $\Delta p = 1000$ Pa between the two GDL surfaces, but may vary significantly under $\Delta p = 6000$ Pa. The water-air interfaces inside the GDL structure were presented to show water distribution and breakthrough.
 [DOI: 10.1149/2.0261809jes]

Manuscript submitted March 14, 2018; revised manuscript received May 15, 2018. Published June 2, 2018.

Proton exchange membrane (PEM) fuel cells offer much promise for replacing the internal combustion engines because of its outstanding merits such as high efficiency, low noise and negligible emissions. The gas diffusion layer (GDL), which provides the transport paths for reactants, is one of the key components in PEM fuel cells.[1] Liquid water in the GDL is originated from the oxygen reduction reaction (ORR) at the cathode catalyst layer, hindering gaseous reactant transport to the catalyst sites. Under severe conditions, electrode "flooding" occurs and may cause material degradation and efficiency reduction. Thus, liquid water needs to be efficiently removed via the GDL to avoid electrode flooding,[2] and predicting the 3D water distribution in the GDL is crucial for fuel cell design and performance optimization.[3]

In general, the GDL is a porous layer composed of woven (carbon cloth) or randomly oriented non-woven carbon fiber (carbon paper),[3,4] as shown in Fig. 1a. A high experimental resolution is extremely necessary for probing water distribution in the GDL that is around 200 μm thick.[5] Presently, two promising imaging techniques are mainly adopted to probe water distribution in GDLs: Neutron radiography[6,7] and X-ray tomography.[8–10] Both techniques are non-destructive to obtain local water content. Cooper et al.[7] employed neutron radiography to examine the local water saturation of an in-situ PEMFC in the direction of through-plane. They found that 3D carbon cloth GDL has lower water saturation than 2D carbon straight fiber paper GDL; Flückiger et al.[8] adopted X-ray tomography microscopy to detect the local water saturation distribution in an ex-situ Toray GDL, they found liquid water retention effect at the denser layers near the surface; Zenyuk et al.[9] used X-ray computed tomography to investigate the land and channel effects on local liquid water distribution in the GDL under different levels of compression, a strong correlation between liquid water saturation and porosity distribution was found at high compression. These imaging techniques are usually costly and time consuming.

Alternatively, several two-phase models have been proposed to predict water dynamics and distribution such as the multiphase mixture (M^2) model,[11–15] lattice Boltzmann method (LBM),[16–20] pore network method (PNM)[21–23] and volume of fluid (VOF) method.[24–26] Pasaogullari et al.[11] presented a M^2 model to predict liquid water profile across the GDL. The Leverett J function was used to estimate the capillary pressure in the GDL. Baschuk and Li[13] adopted a M^2 model to formulate the mass and liquid water transport in the GDL. Wang[15] investigated single- and two-phase regions inside a GDL for both co and counter-flow configurations. They also predicted the liquid water in the anode side. Hao et al.[17] developed a two-phase LBM model to study air-water flow in the GDL's microstructures. They predicted the capillary pressure-water saturation curves in a mixed wettability GDL and compared them with experiments. Agaesse et al.[23] presented a PNM model to perform validation of two-phase flow in the GDL, and a new scheme was proposed for generating the random fiber structures. Park et al.[24] adopted VOF method to investigate water dynamics in the GDL's microstructures, and the effects of fiber contact angle and pressure gradient along the through-plane direction. Yin et al.[25] used a similar approach as Ref. 27 to reconstruct GDLs, and developed a two-phase VOF model to study the effect of non-uniform fiber contact angle on water transport. Importance and theory of multiphase models in PEM fuel cell were discussed by a few reviews and works[1,2,28,29] in detail.

Though various two-phase models have been proposed, few studies compared their prediction of liquid water profile across the GDL with experiment data.[23] One major reason is that those detailed data were only available recently when high-resolution radiography techniques were introduced. In this study, a 3D two-phase VOF model, along with a stochastic model of GDL microstructures reconstruction, was developed to investigate the liquid water distribution inside the Toray carbon paper GDL (TGP-H-060). Although several two-phase VOF models have been adopted for the air-water flow in GDLs,[24–26] model comparison with experimental water profiles in GDLs was mostly ignored. In this study, a major goal is to compare the numerical results of the VOF model with the experimental data obtained from 3D X-ray tomographic microscopy of an ex-situ GDL.[8] The water-air interfaces were presented and water breakthrough was discussed.

Model Development

VOF model.—*Governing equations.*—In the two-phase VOF model, the liquid water phase fraction γ is introduced as a main variable to be solved. The cells fully occupied by liquid water are marked as γ=1, whereas cells fully occupied by air are marked as γ=0. The cells with phase fraction between 0 and 1 consist of air-water interface. The volume averaged density and dynamic viscosity for air-water mixture, ρ and μ, are calculated based on the water phase fraction γ as follows:

$$\rho = \rho_l \gamma + \rho_g (1 - \gamma) \quad [1]$$

$$\mu = \mu_l \gamma + \mu_g (1 - \gamma) \quad [2]$$

where subscripts l and g denote the liquid phase and gas phase respectively. The governing equations for the two-phase VOF model in this study are listed as follows:

*Electrochemical Society Member.
[z]E-mail: yunw@uci.edu; kjiao@tju.edu.cn

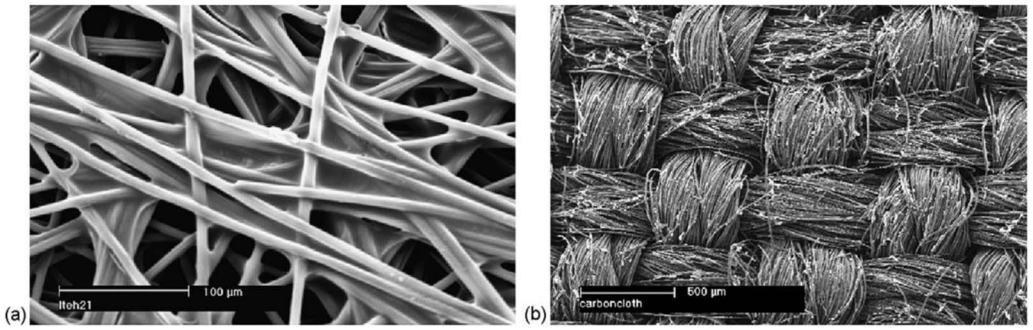

(a)

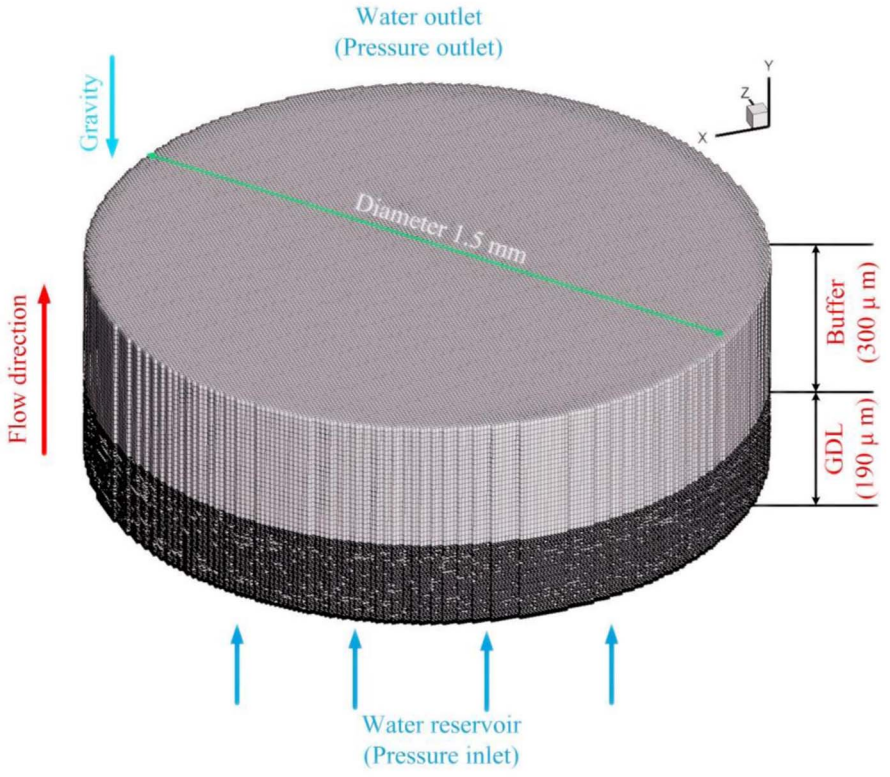

(b)

Figure 1. (a) SEM images of carbon paper and carbon cloth[4] (reprinted from Ref. 4 with the kind permission of the publisher). (b) Computational domain and boundary conditions of two-phase flow within the reconstructed carbon paper model.

Continuity equation:

$$\nabla \cdot \vec{U} = 0 \qquad [3]$$

Phase conservation equation:

$$\frac{\partial \gamma}{\partial t} + \nabla \cdot \left(\vec{U}\gamma\right) + \nabla \cdot \left[\vec{U}_r \gamma (1-\gamma)\right] = 0 \qquad [4]$$

Momentum equation:

$$\frac{\partial(\rho\vec{U})}{\partial t} + \nabla \cdot \left(\rho\vec{U}\vec{U}\right) - \nabla \cdot \left(\mu\nabla\vec{U}\right) - \left(\nabla\vec{U}\right) \cdot \nabla\mu = -\nabla p_d - \vec{g} \cdot \vec{x}\nabla\rho + \sigma\kappa\nabla\gamma \qquad [5]$$

where $\vec{U}$ is the effective velocity vector shared by the two phases throughout the flow domain, which is defined as

$$\vec{U} = \gamma\vec{U}_l + (1-\gamma)\vec{U}_g \qquad [6]$$

$\vec{U}_r = \vec{U}_l - \vec{U}_g$ is the relative velocity of liquid and gas at the interface, designated as "compression velocity", the subscript r here denotes "relative velocity"; γ, σ and κ are the phase fraction, surface tension coefficient and mean curvature of the phase interface, respectively. p_d is a modified pressure for simplifying the boundary conditions, defined as

$$p_d = p - \rho\vec{g} \cdot \vec{x} \qquad [7]$$

where $\vec{x}$ is the position vector and $\vec{g}$ is the gravity vector, the subscript d denotes "dynamic". In this VOF model, the continuum surface force (CSF) model is adopted to account for the effects of surface tension at the liquid-gas interface by adding a force source f_σ to Equation 5, which is defined as follow

$$f_\sigma = \sigma\kappa\nabla\gamma \qquad [8]$$

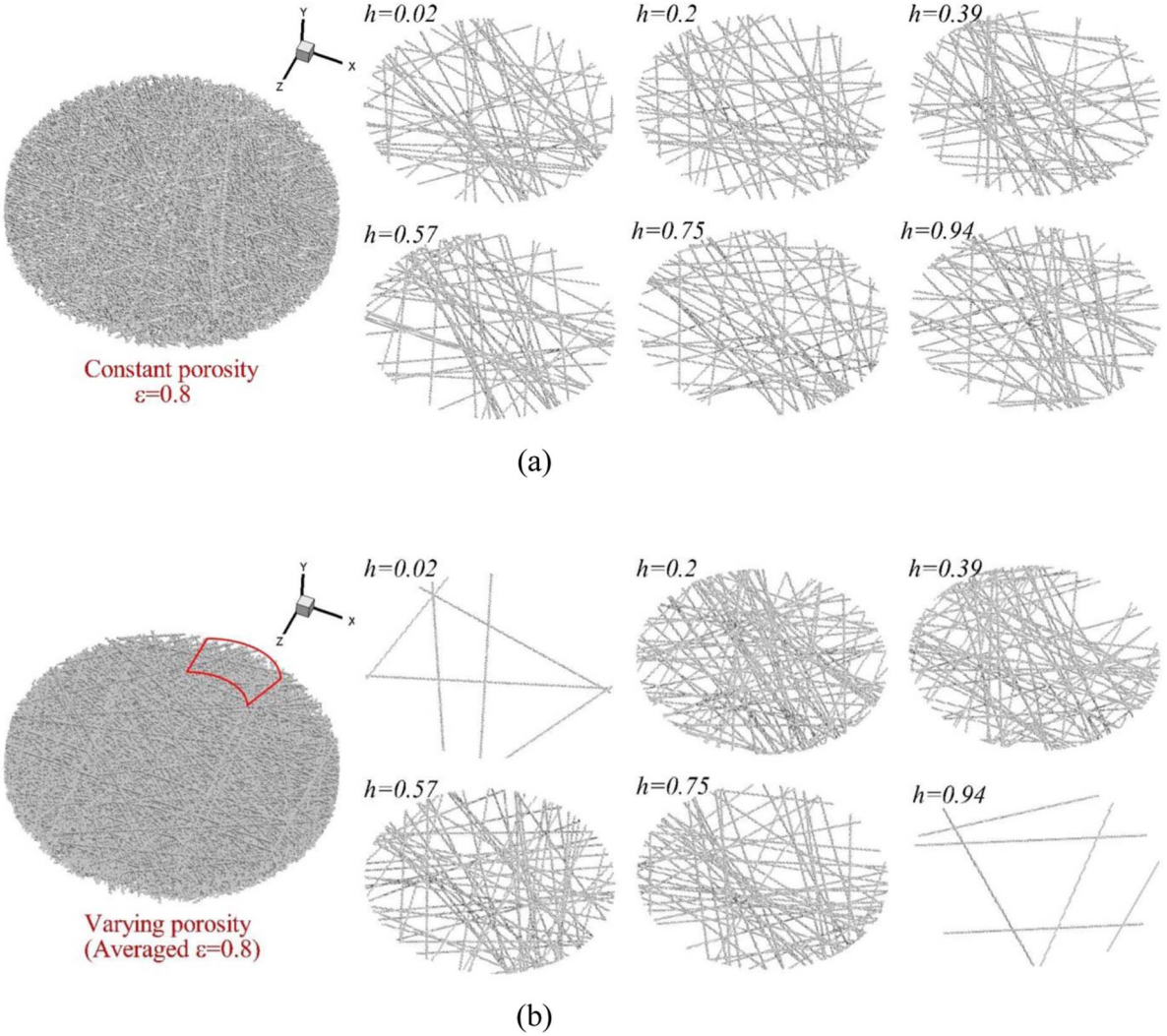

Figure 2. Reconstructed 3D carbon paper and fiber distributions at different in-plane. (a) Constant porosity; (b) Varying porosity (varying porosity distribution is potted in the Fig. 3a).

the subscript σ denotes "surface tension", where the mean curvature of the phase interface κ is determined by:

$$\kappa = -\nabla \cdot \vec{n} = -\nabla \cdot \left(\frac{\nabla \gamma}{|\nabla \gamma|} \right) \quad [9]$$

It can be observed that κ is the interface curvature that is calculated with the divergence of the unit interface normal $\vec{n}$ and the unit interface normal $\vec{n}$ can be approximated with $\nabla\gamma/|\nabla\gamma|$. The surface unit normal $\vec{n}$ is adjusted in the cells adjacent to the wall according to the following equation:

$$\vec{n} = \vec{n}_w \cos\theta + \vec{t}_w \sin\theta \quad [10]$$

where $\vec{n}_w$ is the unit vector normal to the wall, $\vec{t}_w$ is the unit vector tangential to the wall, the subscript w denotes wall. θ is the contact angle. In this study, only the constant contact angle is considered.

Initial and boundary conditions.—The GDL sample in this study is 190 μm thick with a diameter of 1.5 mm. A pressure difference Δp between the inlet and outlet (or the two GDL surfaces) was set, which drives liquid water permeation through the GDL sample. The no-slip boundaries were imposed on the other walls. For no-slip boundary condition, the liquid velocity is set zero at the wall surface. The liquid velocity at the cells adjacent to the wall may not be zero. No-slip boundary is a popular boundary condition set at solid wall surfaces. For example, for liquid flow in a channel/tube, no-slip boundary condition is usually applied at the channel/tube inner surface. A constant fiber contact angle θ, 109° was set for the polytetrafluoroethylene (PTFE) treated (20 wt%) GDL.[30] Initially, there was no liquid water in the GDL.

Numerical procedures.—Because of the complex microstructures and the limited computational mesh, a fiber cross-section is approximated as a square shape, which has been adopted in many previous GDL models.[16–20,25–27] We also conducted a grid-independence study using a small domain, showing the approximation is accurate in predicting two-phase flow in GDLs using the chosen grid size. The computational domain of the present GDL was discretized with 4 million of hexahedral mesh, as shown in Fig. 1b. The open source software Open FOAM was adopted to perform the numerical simulations, and the semi-implicit method for pressure linked equation (SIMPLE) scheme was responsible for the coupling solution of the pressure and velocity. The open-MPI was adopted for parallel computation. The time step was set 2×10^{-7} s. Each case took about 48 hours by using 28 Intel Xeon @2.93 GHz processors in parallel.

Stochastic model.—A Toray carbon paper consists of numerous horizontally orientated straight fibers, as shown in Fig. 1a. The Toray carbon paper TGP-H-060 in the X-ray experiment[8] was

digitally reconstructed using a stochastic method.[17,18,25–27] The following assumptions were made in the digital reconstruction: (i) straightly cylindrical fibers of the same diameter lay in each plane; (ii) fibers are perpendicular to the in-plane direction and can be overlapped with each other; (iii) fibers are randomly distributed in each plane. For the through-plane uniform porosity GDL, in the construction of each plane the same porosity was set. The pore size distribution in the experimental sample was not provided by the original experimental work.[8] However, the pore size distribution of the GDL reconstructed by this commonly used stochastic method has been validated in previous studies.[31–33] For the varying porosity sample, the local porosity of each plane was specified according to the experiment data.[8] Fig. 2 shows a reconstructed carbon paper GDL with spatially constant and varying porosities, respectively. The fiber distributions at different locations are shown in details, and the varying porosity profile in the through-plane direction is plotted in the Fig. 3a. It is seen that the spatially varying porosity case has a larger porosity at the two sides of the GDL and smaller in the middle. In addition, though fibers in each plane were randomly distributed, the pore size is not uniform throughout the plane. Specially, Fig. 2b shows sparse fibers (or relatively large local porosity) at the upper right corner at $h = 0.39$. The GDL of spatially constant porosity was also reconstructed with a porosity $\varepsilon = 0.8$, which is the average of the experimental data.[8]

Results and Discussion

Water through-plane distribution.—This section presents comparison of the local water saturation in the through-plane direction between the model prediction and X-ray experimental data.[8] The local water saturation was obtained by averaging the water phase fraction in the pore space in the in-plane direction. Fig. 3a compares the spatially varying porosity profiles for digitally reconstructed and experimental GDLs.[8] It can be seen that the spatially varying porosities follow similar patterns as the experimental ones with a spatial variation ranging from 0.55 to 0.95. Fig. 3b compares the predicted water profiles with the X-ray experimental data for the three cases. It is noted that the three pressure values of 1000 Pa, 4000 Pa, 6000 Pa refer to the pressure difference Δp between the two GDL surfaces. For the case of 1000 Pa, a rapid drop of the water saturation was indicated near the water entrance in both the experimental data and numerical prediction. After the initial drop, the saturation remains low with little variation. In general, the numerical result agrees well with the experimental data. When the liquid injection pressure increases to 4000 Pa, the prediction shows similar trend as the experimental data, including the beginning fast drop. However, the model prediction shows a slight bump at the middle depth of the GDL, which is absent in the experimental data. For 6000 Pa, the bump near the middle depth in the model prediction is significant, considerably deviating from the experimental data. In addition, the experimental data shows a big jump in the water saturation near the water exit (or right) side of the GDL, where the model only predicted a small increase. The cause for these observed deviations is possibly due to difference in the porosity in-plane variation[9] or the PTFE loading (hence the contact angle) spatial variation.[34] In the range of pressure 1000–6000 Pa, the average water velocity varies from 0 (liquid water fails to break through GDL) to about 0.014 m s^{-1}, which correspond to the water production rate of fuel cell at a current of 0 A cm^{-2} to 7000 A cm^{-2} (normal PEM fuel cell operates up to about 2 A cm^{-2}). For the predicted water velocity larger than normal fuel cell water production rate, we think three points are important to justify the selected range: 1.) Water flow in the cathode GDL may come from other resources, including the anode side via water electroosmosis and water accumulation (or local storage). Water accumulation (or storage) has been observed by other experiments, which leads to periodic liquid break-through GDL.[35] 2.) The experiment paper studied this range of operation (i.e. 1000–6000 Pa) and provided the corresponding image data of water. And 3.) It is also of fundamental importance to investigate general two-phase flows in carbon papers.

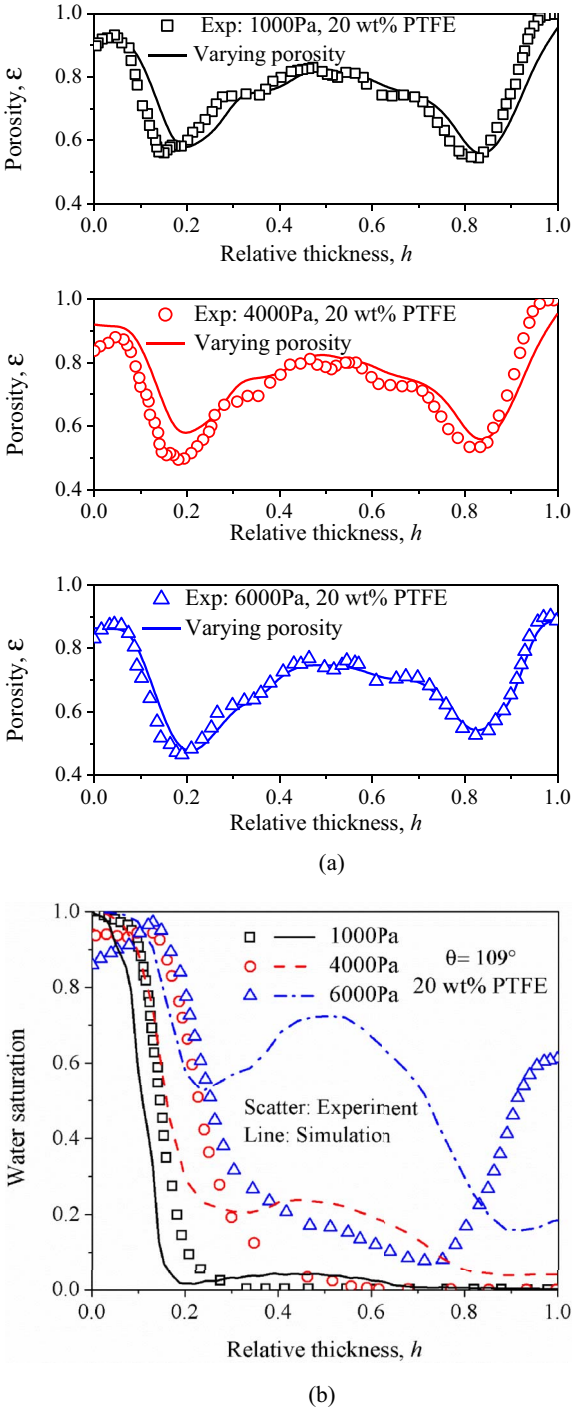

Figure 3. Comparisons of local porosity and water saturation over the through-plane direction between numerical results and X-ray experiment data.[8] Operating conditions: fiber contact angle $\theta = 109°$, 20 wt% PTFE treatment for the GDL, $\Delta p = 1000$, 4000, 6000 Pa. (a) Local porosity; (b) Local water saturation.

Averaged water saturation in GDLs.—Fig. 4 compares the averaged water saturation prediction with experimental data.[8] It can be seen that the model prediction agrees well with the experimental data despite the deviation in the local profiles for 6000 Pa. The model prediction of the uniform porosity GDL is also presented for comparison, showing a large discrepancy with the experimental data. Furthermore, the Leverett J function, a popular correlation for the capillary pressure in porous media, is also plotted. It is seen that under the two low

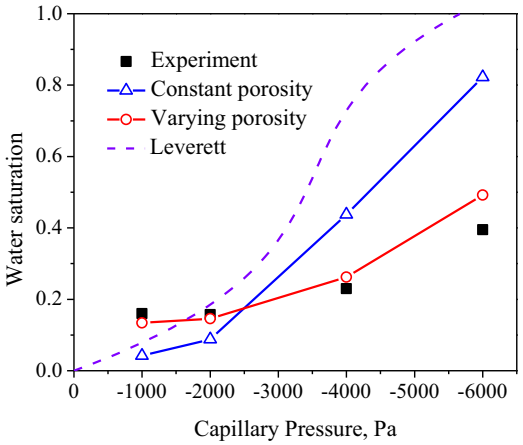

Figure 4. Comparison of numerically averaged water saturation in the entire GDL (both constant porosity and varying porosity) with experimental ones[8] and standard Leverett capillary pressure function model. Operating condition: fiber contact angle $\theta = 109^\circ$, 20 wt% PTFE in GDL, $\Delta p = 1000$ Pa, 2000 Pa, 4000 Pa, 6000 Pa. Parameters for the Leverett capillary pressure function model: Permeability $K = 4.24 \times 10^{-12}$, porosity $\varepsilon = 0.79$, contact angle $\theta = 109^\circ$. The experimental data at 2000 Pa is directly from the Reference 8, while others are calculated from the integral of local water saturation.

pressures the experimental and model data are close to the correlation, while under the two high pressures (i.e. 4000 Pa and 6000 Pa) the correlation gives much higher liquid saturations. This may be due to the unique structure of the GDLs that is different with the random sphere packs for which the Leverett correlation was developed.[36]

Water profiles in GDL sub-regions.—To further explore uniformity in the water profiles, the predicted local saturations in four sub-regions (q1-q4) of the GDLs are plotted in Fig. 5 for both 1000 Pa and 6000 Pa, along with the corresponding local porosity profiles. It can be seen that the porosities vary little among the four selected sub-regions. For 1000 Pa, the saturation profiles are similar among the four sub-regions. We also studied other selections of four sub-regions, which gave similar profiles. For 6000 Pa, a variation of saturation as large as ~0.4 between q3 and q4 is indicated, showing that the liquid water profile may change from region to region. We also found that the variation is dependent on the selection of the sub-regions. It is unclear why the difference is evident for the higher pressure. Further, a small region, qs, is selected to study local porosity and water profiles (also see the highlight in Fig. 2b). It is shown that this site in general has a slightly higher porosity than the four regions, but a significant high water saturation. This location is where water breakthrough occurs, which will be explained in the following section.

Water dynamics in GDLs.—Fig. 6 shows the liquid water dynamics in a cross section and water break-through (characterized by 3D iso-surface of water phase fraction γ=0.5) in the GDL. In the case of $\Delta p = 1000$ Pa, when the flow reaches almost steady state, a thin layer of liquid water is evident near the water entrance region and the majority of the rest part is almost free of water, which agrees with the experimental observation as shown in Fig. 6c. In $\Delta p = 6000$ Pa, liquid water permeates the GDL and fills the bottom part, as shown in Fig. 6b, which is consistent with the experimental observation (Figure 6c). In the model prediction, water penetration took the paths of relatively large local porosity, i.e. the two sides of the constructed GDL where fibers are sparse. Water broke through these regions (highlighted in the pink circle) as a result of the low resistance (or relatively large local porosity[37]) to liquid flow. In contrast, the middle region (highlighted in the green circle) is almost free of water possibly due to presence of local small porosity. In experiment, Fig. 6c shows water break-through occurs near the middle region of the GDL for $\Delta p = 6000$ Pa. It is consistent with Fig. 6b in term of local occurrence of water

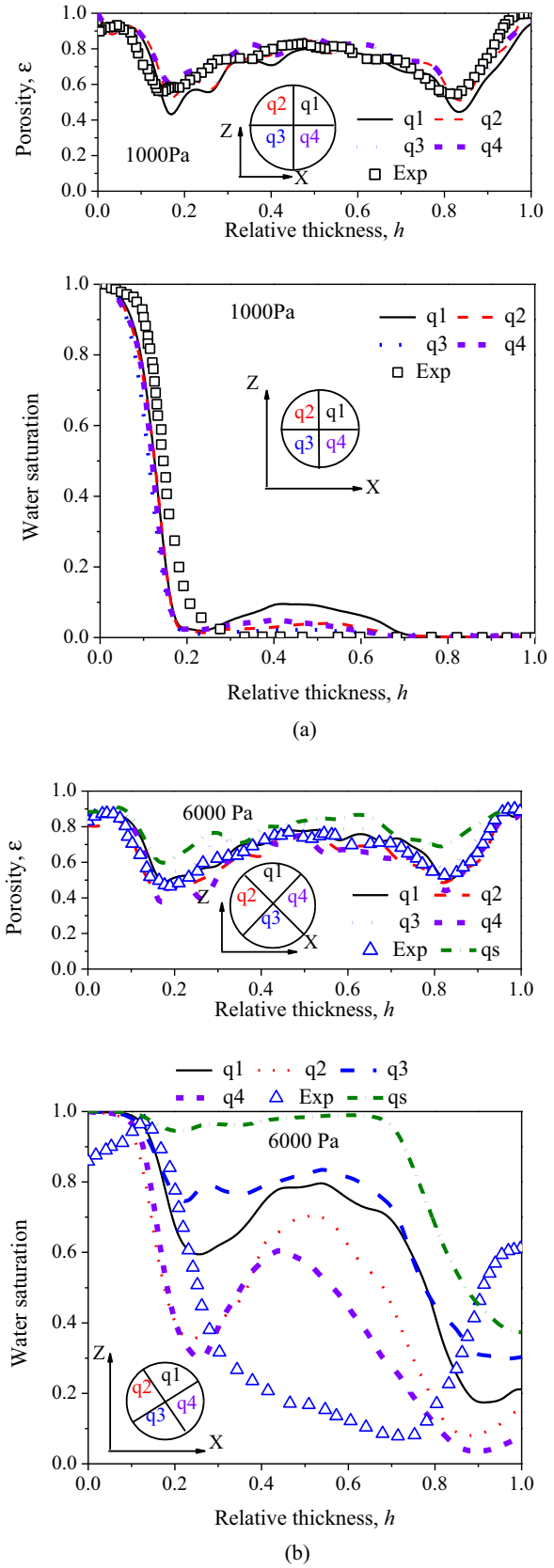

Figure 5. Local porosity and water saturation distribution in different quadrants of the GDL (in-plane) under operating conditions: fiber contact angle $\theta = 109^\circ$, 20 wt% PTFE in GDL, $\Delta p = 1000$, 6000 Pa. (a) Porosity; (b) Local water saturation. It is noted that the region "qs" is highlighted in the Fig. 2.

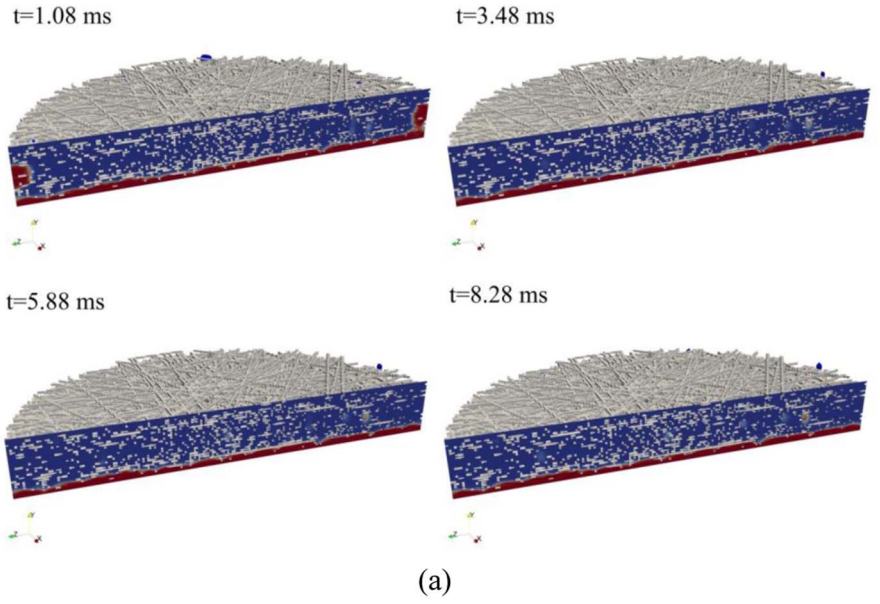

Figure 6. Comparison of the experimental and numerical liquid water dynamics in the through-plane direction (2D slice across the center of the domain) and water break-through (3D iso-surface of water phase fraction γ=0.5) in the GDL. (a) Δp = 1000 Pa; (b) Δp = 6000 Pa; (c) Experimental 3D liquid water distribution. Operating conditions: fiber contact angle $\theta = 109^{\circ}$, 20 wt% PTFE in the GDL (reprinted from Ref. 8 with the kind permission of the publisher). Experimental pictures are obtained from the Reference 8.

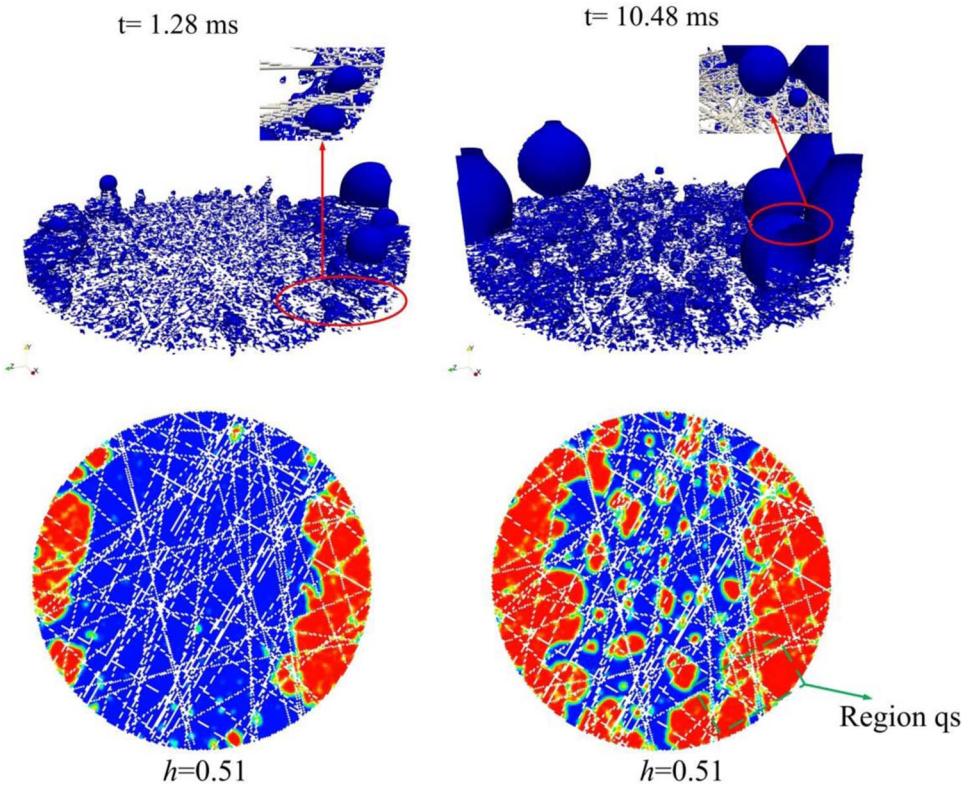

Figure 7. Liquid water flow dynamics in the entirely reconstructed GDL at different time instances (3D iso-surface of water phase fraction γ=0.5 and 2D water phase fraction contour). Operating conditions: fiber contact angle $\theta = 109^{\circ}$, 20 wt% PTFE in GDL, $\Delta p = 6000$ Pa.

breakthrough, but not with the occurring locations. The breakthrough is also determined by local pore size and pore connection,[21,22,37] which were not given in the experiment.[8] Furthermore, this highly localized phenomenon may greatly impact the liquid water profile and the capillary-liquid saturation correlation. A small region (e.g. qs) with a relatively large porosity allows most liquid water to pass through, yielding an overall low saturation as compared with the Leveret correlation. This may also partially explain the discrepancy observed between the predicted profile and experimental data.

Fig. 7 shows details of the liquid water distribution inside the simulated GDL under the operating conditions of $\Delta p = 6000$ Pa. The 3D iso-surface of water phase fraction γ=0.5 is presented to show the two-phase interface location and morphology during water breakthrough. It clearly shows that water penetration occurs at the two sides (right and left) at t = 1.28 ms, when the water content is still small in the rest part in comparison with t = 10.48 ms. In the zoon-in windows, the liquid phase shape is evident when water breaks through the local fiber-constructed throats. At the GDL surface, a partially spherical shape is predicted, as observed by many optical experiments.[38–41] In addition, local water accumulation can be observed in the GDL primarily due to the local large porosity. Water breakthrough in these locations yields water droplet formation at the corresponding GDL surface, which is observed in the experiment in Fig. 6c.

Conclusions

In this study, the air-water flow in gas diffusion layer (GDL) was investigated by a three-dimensional (3D) volume of fluid (VOF) model with the porosity spatial variation taken into account.

1. A stochastic method was employed to reconstruct the microstructure of the GDLs with the through-plane porosity profiles following the experimentally determined data. The local porosity varied from 0.55 to 0.95 across the GDLs.
2. The VOF model was validated with the experimental data from X-ray tomographic microscopy (XTM) in terms of the averaged water saturation as a function of pressure. The pressure-saturation relationship agreed well with the Leverett function under low pressures, i.e. 1000 and 2000 Pa, but gave much smaller liquid saturation under 4000 and 6000 Pa.
3. In the water saturation profile, we found the predicted saturation curves agreed well with the experimental data under 1000 Pa and deviated under 4000 Pa and 6000 Pa. In addition, the water profiles in the four sub-regions of GDLs were found similar with each other under 1000 Pa, but varied considerably under 6000 Pa.
4. Water dynamics insider GDLs were discussed to show the two-phase interface location/shape and water breakthrough. The predicted water distribution in a cross section of the GDL agreed qualitatively with the experimental data for 1000 Pa. For 6000 Pa, the water breakthrough was predicted to occur in a location different with the experiment. It was indicated that the breakthrough site has a relatively large porosity, which may explain the discrepancies observed in the average saturation-pressure relationship and the local saturation profiles.

Acknowledgments

This research is supported by the National Key Research and Development Program of China (grant No. 2016YFB0101303). Y. Wang and J. Wu also thank Shanghai Everpower Technologies Ltd for partial financial support.

ORCID

Zhiqiang Niu https://orcid.org/0000-0001-9220-282X
Yun Wang https://orcid.org/0000-0003-2035-3148

References

1. Y. Wang, K. S. Chen, J. Mishler, S. C. Cho, and X. C. Adroher, *Applied energy*, **88**(4), 981 (2011).
2. K. Jiao and X. Li, *Progress in Energy and Combustion Science*, **37**(3), 221 (2011).
3. M. Mathias, J. Roth, J. Fleming, and W. Lehnert, *Handbook of fuel cells*, (2003).
4. Y. Wang, C.-Y. Wang, and K. Chen, *Electrochimica Acta*, **52**(12), 3965 (2007).
5. A. Bazylak, D. Sinton, Z.-S. Liu, and N. Djilali, *J Power Sources*, **163**(2), 784 (2007).
6. M. Hickner, N. Siegel, K. Chen, D. Hussey, D. Jacobson, and M. Arif, *J Electrochem. Soc.*, **155**(4), B427 (2008).
7. N. J. Cooper, A. D. Santamaria, M. K. Becton, and J. W. Park, *Int J hydrogen energy*, **42**(25), 16269 (2017).
8. R. Flückiger, F. Marone, M. Stampanoni, A. Wokaun, and F. N. Büchi, *Electrochimica Acta*, **56**(5), 2254 (2011).
9. I. V. Zenyuk, D. Y. Parkinson, G. Hwang, and A. Z. Weber, *Electrochemistry Communications*, **53**, 24 (2015).
10. A. Lamibrac, J. Roth, M. Toulec, F. Marone, M. Stampanoni, and F. Büchi, *J Electrochem. Soc.*, **163**(3), F202 (2016).
11. U. Pasaogullari and C.-Y. Wang, *J Electrochem. Soc.*, **152**(2), A380 (2005).
12. U. Pasaogullari, C.-Y. Wang, and K. S. Chen, *J Electrochem. Soc.*, **152**(8), A1574 (2005).
13. J. Baschuk and X. Li, *J Power Sources*, **142**(1-2), 134 (2005).
14. N. Zamel and X. Li, *Int J Energy Research*, **32**(8), 698 (2008).
15. Y. Wang, *J Power Sources*, **185**(1), 261 (2008).
16. F. Jinuntuya, M. Whiteley, R. Chen, and A. Fly, *J Power Sources*, **378**, 53 (2018).
17. L. Hao and P. Cheng, *Int J Heat and Mass Transfer*, **55**(1-3), 133 (2012).
18. L. Chen, H.-B. Luan, Y.-L. He, and W.-Q. Tao, *Int J Thermal Sciences*, **51** 132 (2012).
19. S. Sakaida, Y. Tabe, and T. Chikahisa, *J Power Sources*, **361**, 133 (2017).
20. Z. Liu and H. Wu, *Int J Hydrogen Energy*, **41**(28), 12285 (2016).
21. M. Shahraeeni and M. Hoorfar, *Int J Hydrogen Energy*, **39**(20), 10697 (2014).
22. B. Straubhaar, J. Pauchet, and M. Prat, *Int J Heat and Mass Transfer*, **102**, 891 (2016).
23. T. Agaesse, A. Lamibrac, F. N. Büchi, J. Pauchet, and M. Prat, *J Power Sources*, **331**, 462 (2016).
24. J. W. Park, K. Jiao, and X. Li, *Applied Energy*, **87**(7), 2180 (2010).
25. Y. Yin, T. Wu, P. He, Q. Du, and K. Jiao, *Int J Hydrogen Energy*, **39**(28), 15772 (2014).
26. Z. Niu, K. Jiao, Y. Wang, Q. Du, and Y. Yin, *Int J Energy Research*, **42**, 802 (2018).
27. V. P. Schulz, J. Becker, A. Wiegmann, P. P. Mukherjee, and C.-Y. Wang, *J Electrochem. Soc.*, **154**(4), B419 (2007).
28. Y. Wang and K. S. Chen, *PEM fuel cells: thermal and water management fundamentals*, Momentum Press (2013).
29. P. P. Mukherjee, Q. Kang, and C.-Y. Wang, *Energy & Environmental Science*, **4**(2), 346 (2011).
30. D. L. Wood, C. Rulison, and R. L. Borup, *J Electrochem. Soc.*, **157**(2), B195 (2010).
31. M. Hannach and E. Kjeang, *J Electrochem. Soc.*, **161**(9), F951 (2014).
32. P. Mukherjee, C. Wang, and Q. Kang, *Electrochimica Acta*, **54**, 6861 (2009).
33. S. Simaafrookhteh, M. Shakeri, M. Baniassadi, and A. Sahraei, *Fuel Cells*, **18**, 160 (2018).
34. H. Ito, K. Abe, M. Ishida, A. Nakano, T. Maeda, T. Munakata, H. Nakajima, and T. Kitahara, *J Power Sources*, **248**, 822 (2014).
35. C. Hartnig, I. Manke, R. Kuhn, S. Kleinau, J. Goebbels, and J. Banhart, *J Power Sources*, **188**, 468 (2009).
36. M. Leverett, *Transactions of the AIME*, **142**(01), 152 (1941).
37. Y. Wang and K. S. Chen, *J Electrochem. Soc.*, **158**(11), B1292 (2011).
38. Y. Wang, *J Electrochem. Soc.*, **156**(10), B1134 (2009).
39. S. C. Cho, Y. Wang, and K. S. Chen, *J Power Sources*, **210**, 191 (2012).
40. F. Zhang, X. Yang, and C. Wang, *J Electrochem. Soc.*, **153**(2), A225 (2006).
41. A. Theodorakakos, T. Ous, M. Gavaises, J. Nouri, N. Nikolopoulos, and H. Yanagihara, *J colloid and interface science*, **300**(2), 673 (2006).